Title

Single-molecule detection of protein efflux from microorganisms using fluorescent single-walled carbon nanotube sensor arrays

Journal

Nature Nanotechnology, 12(4)

ISSN

1748-3387

Authors

Landry, Markita Patricia
Ando, Hiroki
Chen, Allen Y
et al.

Publication Date

2017-04-01

DOI

10.1038/nnano.2016.284

Peer reviewed

nature nanotechnology

ARTICLES

PUBLISHED ONLINE: 23 JANUARY 2017 | DOI: 10.1038/NNANO.2016.284

Single-molecule detection of protein efflux from microorganisms using fluorescent single-walled carbon nanotube sensor arrays

Markita Patricia Landry[1,2], Hiroki Ando[3,4], Allen Y. Chen[3,4,5], Jicong Cao[3,4], Vishal Isaac Kottadiel[6,7], Linda Chio[1], Darwin Yang[1], Juyao Dong[8], Timothy K. Lu[3,4] and Michael S. Strano[8]*

A distinct advantage of nanosensor arrays is their ability to achieve ultralow detection limits in solution by proximity placement to an analyte. Here, we demonstrate label-free detection of individual proteins from *Escherichia coli* (bacteria) and *Pichia pastoris* (yeast) immobilized in a microfluidic chamber, measuring protein efflux from single organisms in real time. The array is fabricated using non-covalent conjugation of an aptamer-anchor polynucleotide sequence to near-infrared emissive single-walled carbon nanotubes, using a variable chemical spacer shown to optimize sensor response. Unlabelled RAP1 GTPase and HIV integrase proteins were selectively detected from various cell lines, via large near-infrared fluorescent turn-on responses. We show that the process of *E. coli* induction, protein synthesis and protein export is highly stochastic, yielding variability in protein secretion, with *E. coli* cells undergoing division under starved conditions producing 66% fewer secreted protein products than their non-dividing counterparts. We further demonstrate the detection of a unique protein product resulting from T7 bacteriophage infection of *E. coli*, illustrating that nanosensor arrays can enable real-time, single-cell analysis of a broad range of protein products from various cell types.

There is significant interest in the label-free optical detection of proteins from crude, unpurified biological samples, or directly from the protein production source. Protein expression and secretion guide a significant aspect of nearly every cellular metabolic or signalling pathway. In some systems, stochasticity in protein production is inherent. In other systems, aberrations in protein expression can be representative of disease states. In both cases, detection of protein from crude samples, or from the point of production, could significantly reduce the time necessary to detect variability or aberrations in protein production[1]. To detect and quantify protein expression and secretion, standard approaches rely primarily on immunological analytical methods including enzyme-linked immunosorbent assays (ELISA), western blotting, radial immunodiffusion, or mass spectrometry. Recent advances have explored electrochemical detection of proteins with antibodies and aptamers, with great success for temporal quantification of protein from purified samples, several with picomolar detection capabilities[2–5]. Fluorescence labelling of target proteins has provided the additional dimension of spatial information for protein detection and studying protein–protein interactions, although most protein detection strategies are for intracellular protein detection[6–8]. However, such methods rely on fluorescent modification of the target protein and are restricted to use inside the cell. Moreover, these approaches for protein detection and quantification often require preliminary purification steps before analysis, further elongating the time between protein production and detection.

In light of the need for label-free spatiotemporal optical detection of proteins in complex biological environments, we have developed a sensitive and selective label-free protein detection platform imaged with a custom-built near-infrared microscope[9,10]. We base this platform on the coupling of aptamer-anchor polymers to semiconducting single-walled carbon nanotube (SWNT) near-infrared (nIR) emitters. This platform leverages the selectivity for specific protein targets via synthetic DNA aptamers adhered to SWNTs. DNA aptamers for proteins are selected from reported systematic evolution of ligands by exponential enrichment polynucleotide segments with known affinities for protein targets. Protein binding to aptamer targets on SWNTs subsequently relays an optical signal in the nIR optical window. Photon scattering in biological samples is low in the nIR emission window, enabling, optical detection of single proteins in complex biological media such as crude cell lysates and bacterial cultures. Furthermore, SWNTs are the only fluorophores to date that have essentially infinite lifetimes and are not susceptible to on–off blinking, as quantum dots are. Therefore, the signal produced by SWNTs, combined with the selectivity provided by aptamers, provides much promise for the long-term optical monitoring of specific protein targets from within crude biological samples over long timescales.

Here, we (1) develop a platform to optically detect specific proteins, and (2) detect proteins of interest from unpurified crude cell lysates. We show the immediate utility of our platform by (3) detecting single secreted proteins from *Escherichia coli*, HEK 293 and *Pichia pastoris* cells engineered to synthesize and secrete our

[1]Department of Chemical and Biomolecular Engineering, University of California Berkeley, Berkeley, California 94720, USA. [2]California Institute for Quantitative Biosciences (qb3), University of California-Berkeley, Berkeley, California 94720, USA. [3]Department of Electrical Engineering & Computer Science and Department of Biological Engineering, Massachusetts Institute of Technology, Cambridge, Massachusetts 02139, USA. [4]MIT Synthetic Biology Center, Massachusetts Institute of Technology, Cambridge, Massachusetts 02139, USA. [5]Biophysics Program, Harvard University, Cambridge, Massachusetts 02138, USA. [6]The Rowland Institute at Harvard University, Cambridge, Massachusetts 02142, USA. [7]Department of Biology, The Catholic University of America, Washington, District of Columbia 20064, USA. [8]Department of Chemical Engineering, Massachusetts Institute of Technology, Cambridge, Massachusetts 02138, USA. *e-mail: strano@mit.edu

protein target upon induction and show that a single cell's protein secretion 'footprint' depends on whether it is undergoing cell division. Finally, we (4) monitor the real-time lytic release of target protein from cells infected with a T7 bacteriophage engineered to transfect our target protein gene into its bacterial host, for various multiplicity of infection (MOI) ratios. We thereby confirm that the relationship between T7 infection-to-lysis time and viral load follows a power-law relationship.

Aptamer-anchor design for selective protein recognition

We can engineer an optical response to a protein target via aptamer-anchoring to SWNT surfaces. Aptamers are nucleotide polymers with a high sequence-specific affinity for a particular target molecule, often a protein. The polymer for this platform is based on an 'anchor' domain that adheres the polymer to the SWNT surface[11,12] and a molecular recognition 'capture' domain that enables selective perturbation of the SWNT fluorescence[13–15] by only the conjugate protein target. Here, the anchor segments are alternating AT nucleotide repeats that have been shown to adsorb strongly to the SWNT surface[16], and the molecular recognition is provided by a folded polynucleotide aptamer. In this manner, unlabelled proteins can be detected with SWNTs via DNA heteropolymers with $(AT)_{11}$ DNA 'anchor' sequences and aptamer 'binding domains' (Fig. 1a).

We tested this platform by constructing an aptamer-anchor SWNT sensor for RAP1 protein, a vital cytosolic protein for T-cell receptor signalling. Following the addition of 3 μM purified RAP1 protein to solution-phase sensor, RAP1 docks to the aptameric binding domain of our sensor and we observe a 53% increase in the normalized SWNT intensity, $((I - I_o)/I_o)$ (Fig. 1a). The proximity of the protein to the SWNT surface produces a change in the local dielectric environment of the SWNT, which produces a nIR optical signal in the form of a SWNT fluorescence increase. We next probed the generalizability of our platform to a library of proteins and their aptameric targets conjugated to SWNTs. We constructed a library of nine SWNT–aptamer sensors and screened them against their conjugate proteins as well as the other non-target proteins in the library. The protein concentrations added varied from 110 nM to 6.6 μM, depending on the biologically relevant concentration of each protein (see Supplementary Section 'Methods'). Figure 1b shows the fluorescence response heat map for each pair, as a function of the SWNT normalized intensity $((I - I_o)/I_o)$. Two aptamer–SWNT sensors, in particular, respond strongly and selectively to their protein targets: RAP1 and HIV1 integrase, which show 53 and 48% fluorescence turn-on responses in the presence of their protein targets, respectively. Off-diagonal non-specific cross-responses were not observed. We subsequently performed a series of experiments to understand the response mechanism of our sensors.

To better understand which aspects of our sensors yield strong and selective fluorescence signals to their conjugate proteins, we constructed three chemical variants of each anchor-aptamer polymer by incorporating either one, three or five consecutive 18-atom hexa-ethyleneglycol spacers between the $(AT)_{11}$ anchor sequence and the aptamer sequence. The spacers are abasic and do not adsorb onto the SWNT surface, creating a physical separation between the SWNT surface anchor and aptamer sequence, where the physical length of a single spacer is ~1.3 nm.

Our results show that the incorporation of one or three abasic spacers between the anchor and RAP1 aptamer domains drastically improves our sensor response. Alternatively, removal of the $(AT)_{11}$ anchor sequence abolishes the sensor response and produces unstable DNA–SWNT suspensions (Supplementary Fig. 1). The response of each of the one and three abasic spacer SWNT sensors increases nearly fourfold compared to a sensor without a spacer. These results suggest that one or three spacers distance the aptamer to disfavour aptamer adhesion to the SWNT surface, while keeping the aptamer within the dielectric environment of the SWNT surface that enables perturbation of the fluorescence emission. In contrast, when incorporating one, three or five abasic spacers between the anchor and aptamer sequence of the thrombin polymer, no response is observed, similar to the construct without a spacer (Fig. 1c). This could be a result of a strongly adherent thrombin aptameric sequence that will not desorb from the SWNT surface. It is also possible that the binding of thrombin to the aptamer near the surface of the SWNT does not sufficiently perturb the SWNT dielectric environment to produce a change in the SWNT fluorescence.

To probe the structure of the aptamer in the case of the responsive RAP1 sensor compared to the non-responsive thrombin sensor, we designed a series of single-molecule experiments. We tagged each of our $(AT)_{11}$–RAP1 and $(AT)_{15}$–thrombin sequences with a 3′ terminal Cy3 dye, which is known to quench as a function of proximity to the surface of the SWNTs[17,18]. The predominant structure of the aptamer was then tested by surface-immobilizing our SWNT sensors on the surface of a microfluidic chamber (see Supplementary Section 'Methods') and observing the number of fluorescent spots observed following excitation of the Cy3 dye. For Cy3-tagged RAP1 sensors, addition of the complementary sequence resulted in no significant net increase in Cy3 emitters (from 43.2 ± 3.8 pre-$(AC)_6$ to 44.0 ± 2.6 post-$(AC)_6$ (mean ± s.e.)). In contrast, for Cy3-tagged thrombin sensors, addition of the complementary sequence resulted in a significant net increase in Cy3 emitters (from 18.3 ± 1.3 pre-$(AC)_6$ to 66.0 ± 4.6 post-$(AC)_6$ (mean ± s.e.); Fig. 1d). These results, along with both positive and negative controls (see Supplementary Fig. 2) suggest that the RAP1 aptamer is primarily found in its correctly folded G-quadruplex structure, whereas the thrombin aptamer is primarily stacked onto the SWNT surface.

Unlabelled protein detection from crude cell lysates

We quantified the sensitivity of our RAP1 aptamer sensor by surface-immobilizing our sensors and flowing in varying concentrations of recombinant human RAP1 protein (Abcam, ab162732). On flowing in RAP1, an immediate increase in fluorescence intensity $((I - I_o)/I_o)$ was observed for all sensors in our field of view, with $(I - I_o)/I_o$ ranging from 0.73 ± 0.06 to 1.82 ± 0.08 (mean ± s.e.) for 0.25 μg ml^{-1} and 25 μg ml^{-1} RAP1 protein, respectively (Fig. 2a). We observed this turn-on signal simultaneously from all sensors in our field of view, at all concentrations (Fig. 2b), except for sensors exposed to 0.25 μg ml^{-1} RAP1 protein (Fig. 2c). At 0.25 μg ml^{-1}, the response observed was primarily that of individual aptamer–SWNT sensors turning on independently and often reversibly (Fig. 2d). Given the molecular mass of our RAP1 protein (~30 kDa), this corresponds to a protein concentration of 3.5 nM, well within a single-molecule concentration regime. We developed a model based on intensity response for the bulk-response regime and the first passage time response for the single-sensor regime, to explain the response profile of our sensor as a function of RAP1 concentration (see Supplementary Information for the Model for sensor response to RAP1 protein *in vitro*) and fit it to our experimental concentration curves.

Our aptamer–protein screen in Fig. 1b shows the promise of selectivity in the use of aptamer–SWNT sensors to detect proteins from complex molecular environments. We next tested the ability of our RAP1 aptamer sensor to function amid other biomolecules. We first performed a screen for the RAP1 aptamer–SWNT sensor response to two proteins that are known to bind to exposed surfaces of DNA–SWNT constructs: bovine serum albumin and neutravidin. Neither protein produced a significant change in the fluorescence of the RAP1 aptamer–SWNT (Supplementary Fig. 3). Next, we tested the RAP1 aptamer–SWNT sensor for its ability to detect RAP1 from

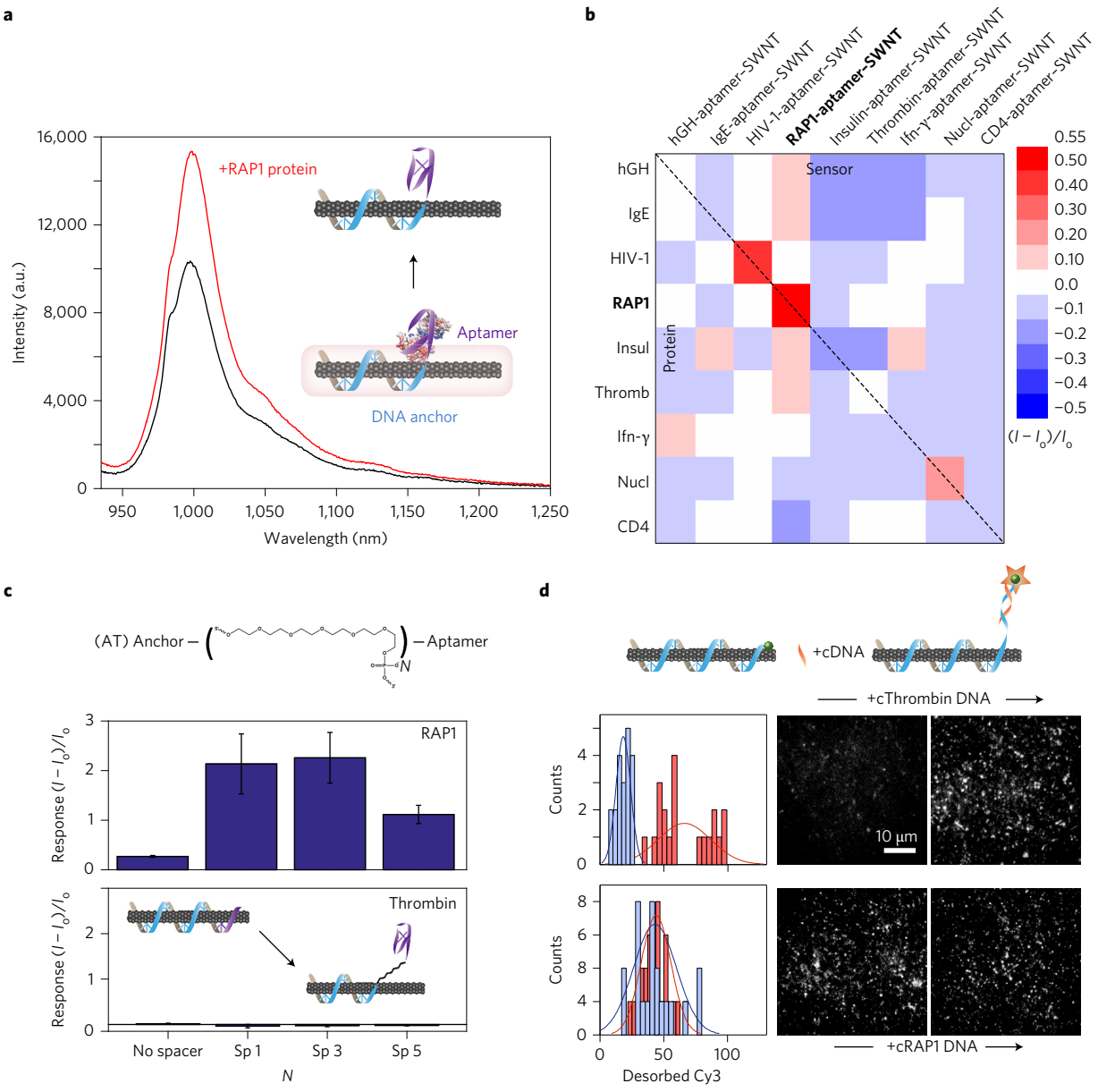

Figure 1 | Characterization of the aptamer-anchor structure on nanotube. a, 6,5-Chirality RAP1 aptamer–SWNT response to the addition of 3 μM RAP1 protein, with a schematic representation of aptamer–SWNT construct binding, with the DNA anchor in blue and the DNA or RNA aptamer in purple. **b**, Nine aptamer–SWNT screen (horizontal axis) against nine protein analytes (vertical axis). Red is sensor fluorescence turn-on, blue is sensor fluorescence turn-off, where off-diagonal elements represent the SWNT fluorescence response to non-conjugate (non-specific) protein–aptamer SWNT pairs and the diagonal (highlighted by a dashed black line) represents the fluorescence response to conjugate (specific) protein–aptamer SWNT pairs. We observe strong turn-on responses (red) for RAP1 protein and HIV1 integrase protein, with normalized fluorescence turn-on responses of $(I - I_o)/I_o = 0.53$ and 0.48, respectively. **c**, RAP1 (top) aptamer–SWNT constructs with $N = 1$, 3 or 5 abasic spacers between anchor and aptamer detect RAP1 with a larger fluorescence turn-on response than constructs lacking a spacer. The response for thrombin (bottom), however, is unchanged, regardless of spacer incorporation. Results suggest an aptamer equilibrium that fluctuates between a correctly folded aptamer (protein accessible) on the SWNT and an incorrectly folded aptamer (protein inaccessible) on the SWNT surface. Error bars represent standard error (s.e.). **d**, Single-molecule total internal reflection fluorescence (TIRF) visualization of the aptamer–SWNT interaction for Cy3-labelled RAP1. The Cy3 tag on the thrombin SWNT sensor is initially quenched (top, blue histogram), suggesting the thrombin aptamer is denatured on the SWNT. Addition of ssDNA complementary to the thrombin aptamer, +cThrombin DNA, de-quenches the Cy3 tag and leads to an increase in visible Cy3 fluorophores (red histogram). Conversely, the Cy3 tag on the RAP1 SWNT sensor is initially de-quenched (bottom, blue histogram), suggesting the RAP1 aptamer is properly folded on the SWNT. Addition of ssDNA complementary to the RAP1 aptamer, +cRAP1 DNA, does not change the Cy3 count (red histogram). The results suggest a primarily SWNT surface-desorbed RAP1 aptamer and primary SWNT surface-adsorbed thrombin aptamer.

crude *E. coli* cell lysates. The RAP1 gene was transfected into *E. coli* BL21 cells and cells were isopropyl β-D-1-thiogalactopyranoside (IPTG)-induced to produce RAP1 protein (Fig. 3a). A control batch of cells lacking the RAP1 gene insertion was also prepared. Each sample was lysed in a sonicator, and the crude lysate was isolated by centrifugation (see Supplementary Section 'Methods'). We next immobilized the RAP1 aptamer–SWNT sensor on the surface of a microfluidic chamber and monitored the nIR fluorescence response of our surface-immobilized sensors following the addition of a 1:100 dilution of RAP1-transfected *E. coli* cell lysate and the RAP1-free control cell lysate. Immediately following the addition of the crude RAP1 cell lysate supernatant dilution, we observed an

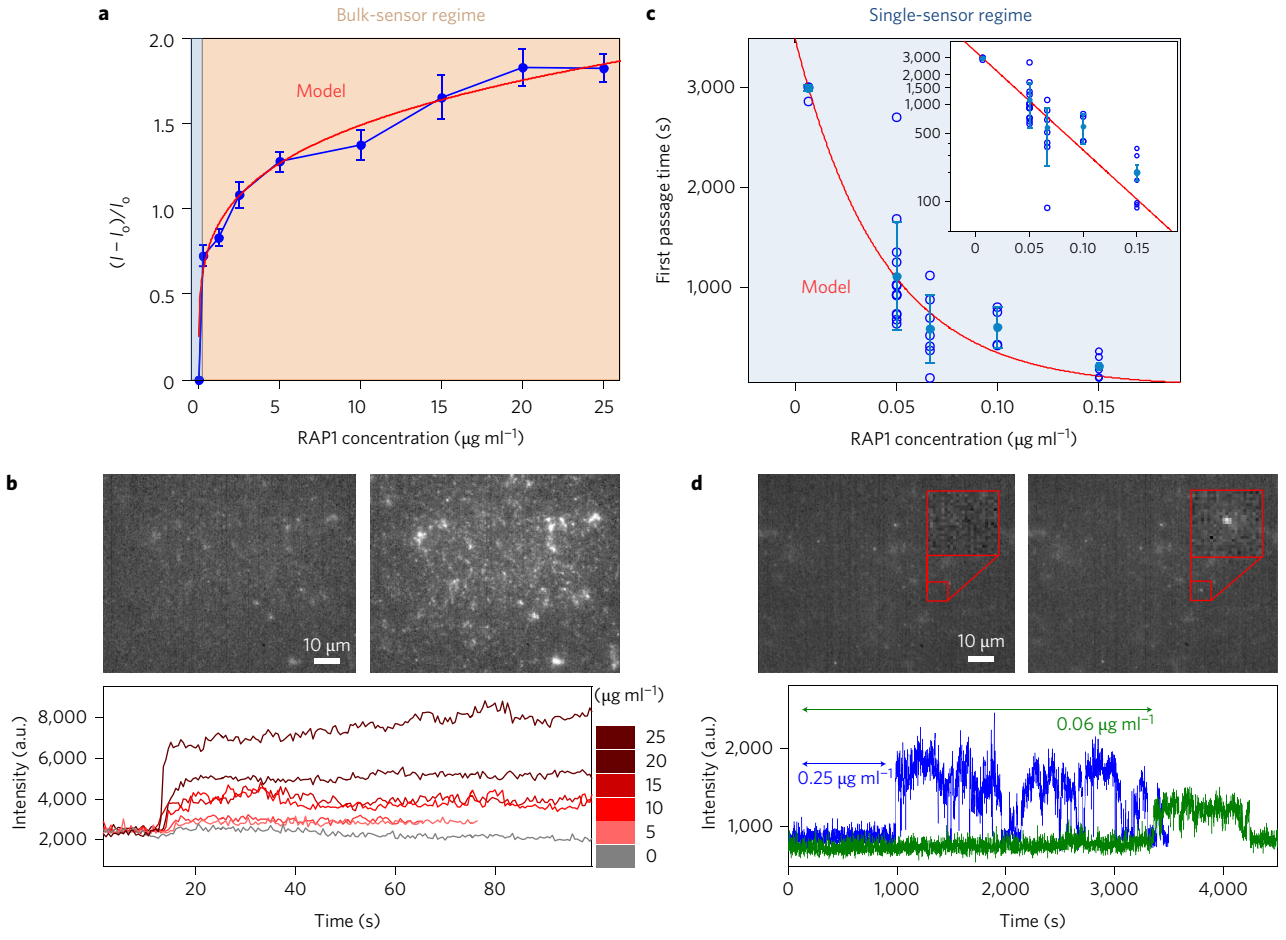

Figure 2 | Calibration of nanosensor response to recombinant protein. a, Concentration–response curve for RAP1 protein, showing two regimes of response. Above 0.15 μg ml^{-1} RAP1, a bulk sensor response is observed for the integrated sensor response for all sensors in the field of view (red), whereas below 0.15 μg ml^{-1} RAP1, individual sensor responses are observed (blue). **b**, Example nIR intensity response following the addition of RAP1 and corresponding integrated intensity curves for RAP1 concentrations from 0 to 25 μg ml^{-1}. **c**, First passage time until first sensor turn-on response at various RAP1 concentrations within the single-senor response regime. First passage times show a decaying exponential, as expected from protein diffusion-limited kinetics, with semilog (y) plot inset. **d**, Example single-sensor nIR intensity response following the addition of RAP1 protein (red box). Sample traces are shown to demonstrate variance in first passage times for two sample RAP1 concentrations, 0.25 μg ml^{-1} (blue) and 0.06 μg ml^{-1} (green). All error bars are standard error. Sensor sensitivity can measure individual binding events in the single-sensor regime.

increase in sensor intensity $((I - I_o)/I_o) = 1.7$ within the 0.5 s frame acquisition rate of our microscope (Fig. 3b). The increase in fluorescence is notably absent in the crude cell lysate lacking RAP1 expressed protein $((I - I_o)/I_o) = -0.1$. Because our platform has single-protein sensitivity, if a generating source, instead of a pool, of individual proteins is to be placed in the proximity of the sensor array, a singular protein could be detected within the 200 μl sample volume of our chamber. Because one protein = 1.66×10^{-24} moles, within our 200 μl sample volume, a source generating single proteins can be used to achieve effectively zeptomolar (1.66×10^{-24} moles per 200 μl) protein detection, although the analyte arrival time is a better metric of sensitivity in this stochastic limit. We explore this in subsequent measurements of proteins from individual live cells.

Real-time detection of protein secreted from *E. coli*

We engineered *E. coli* to express and secrete RAP1 peptide upon induction with anhydrotetracycline (aTc), as described previously[19,20]. We tested the response of our protein sensor platform by introducin a titration of RAP1-secreting *E. coli* concentrations into our microfluidic chambers. For *E. coli* concentrations of 1×10^8 c.f.u. ml^{-1} (c.f.u., colony-forming units) to 1.6×10^9 c.f.u. ml^{-1}, a bulk sensor response is observed across the entire sensor surface field of view, as expected from the dense packing of *E. coli* cells observed in the corresponding bright-field view of our microfluidic chamber (Fig. 3c). For *E. coli* concentrations of $\sim 1.5 \times 10^7$ c.f.u. ml^{-1}, the bright-field view of our chamber shows sparse dispersions of *E. coli* cells, approximately one cell found per $\sim 60 \times 80$ μm^2 field of view. At this low cell concentration, we limited the mobility of individual *E. coli* cells within the microfluidic chamber to allow for an hour-long observation of the same cell and induced this cell with aTc (see Supplementary Section 'Methods'). After a time lag attributed to protein transcription and translation, we observed individual RAP1 aptamer–SWNT sensor responses following RAP1 protein efflux from individual *E. coli* cells. From our sensor response calibration curve and the corresponding model (Fig. 2), we can attribute the single-sensor responses to the binding of a RAP1 protein to an aptameric docking site near the SWNT. Figure 3c shows a representative bulk turn-on response of our surface-immobilized sensors when *E. coli* concentrations of 1×10^8 c.f.u. ml^{-1} to 1.6×10^9 c.f.u. ml^{-1} are introduced into the microfluidic chamber. Conversely, Fig. 3d shows representative single-sensor turn-on responses as the result of protein secretion from a single immobilized *E. coli* cell. The *E. coli* cell in Fig. 3d behaves as a protein generation source within our microfluidic chamber. We note that the ability of the array to monitor singular protein efflux from the *E. coli* source within the 200 μl chamber

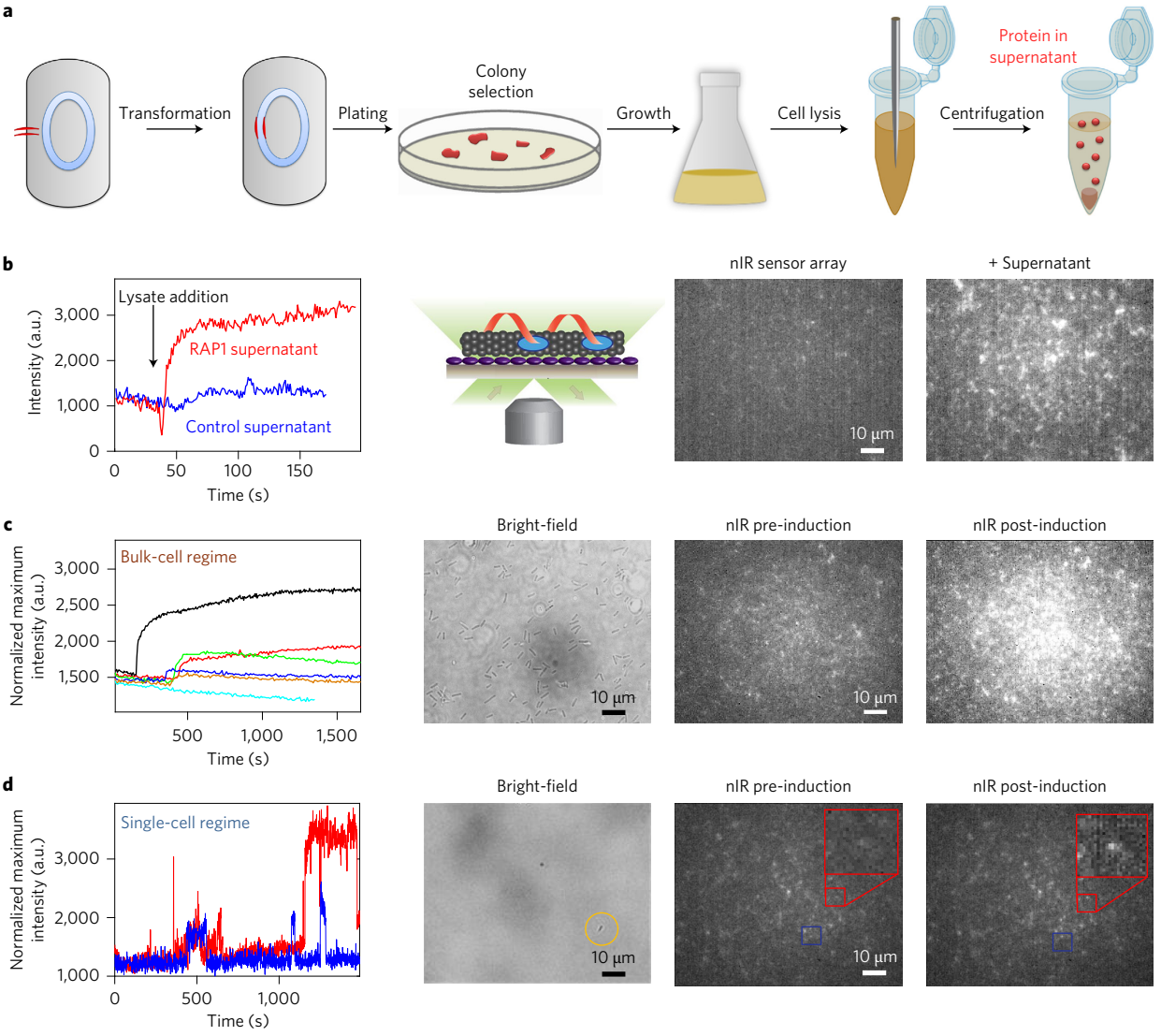

Figure 3 | Detection of protein from crude cell lysate and from *E. coli* engineered to secrete target protein. a, Schematic of RAP1 transformation and *E. coli*$_{RAP1}$ growth. **b**, Surface-immobilized RAP1 aptamer–SWNT sensors (schematic) show an instantaneous turn-on response following the addition of crude cell lysate from cells grown to produce RAP1. The fluorescence of crude cell lysate from cells lacking the RAP1 gene remains largely invariant. **c**, Concentration–response curves for 0 (cyan), 1×10^8 (orange), 4×10^8 (blue), 7×10^8 (red), 1×10^9 (green) and 1.6×10^9 (black) c.f.u. ml^{-1} *E. coli* engineered to secrete RAP1 and corresponding sensor nIR responses before and post-induction with 50 nM aTc. **d**, Two representative single-sensor fluorescence intensity traces (red and blue) for an agarose gel-immobilized *E. coli* bacterium, circled yellow in the bright-field image, engineered to secrete RAP1. Also shown are corresponding nIR intensity images of surface-immobilized sensors (boxed in red and blue) pre- and post-induction with aTc.

effectively demonstrates a 8.3 zeptomolar (1.66×10^{-24} moles per 200 μl) protein detection, although in reality, the concentration no longer limits detection in this stochastic limit, but rather the analyte arrival time as in Fig. 2c.

Protein detection from single *E. coli*, HEK 293 and *P. pastoris* cells

We studied $N = 22$ individual *E. coli* cells from induction through the course of an hour. We did so as described above and as depicted in Fig. 4a, by casting a low concentration of *E. coli* in 0.2% agarose minimal media above a dense array of our RAP1 protein nanosensors. We subsequently model our system, as depicted in Fig. 4a, for each of four discrete stages of RAP1 model protein detection from our *E. coli* cells. Our model begins with the introduction of inducer aTc into our single-cell-containing matrix at $t = 0$, through observation of secreted proteins at our sensor array: I—introduction of aTc into the cell matrix and diffusion into the cell; II—expression (transcription of gene and translation of product); III—secretion of protein; and IV—diffusion of protein to the sensor array. With the exception of protein secretion (step III), a process that has not yet been studied in the literature at the single-cell and single-protein level, each of these mechanisms can be modelled with diffusion kinetics (steps I and IV), or derived kinetically from the literature (step II). Step I, diffusion of aTc to the *E. coli* cell, is described by the Brownian diffusion of the aTc inducer through the agarose matrix to the cell and is calculated to be near instantaneous at 0.4 s, as described by the sharp peak in Fig. 4c. Step II, the transcription, translation and intracellular diffusion of RAP1, has been detailed in the literature. We combine the literature values of the transcription and translation rates for *E. coli* to model the timing of RAP1 production, also considering the depletion of mRNA and protein that is likely to occur in a carbon-source-depleted environment such as the minimal media in which our experiments are conducted (Fig. 4c, dotted lines). Step III, the secretion of RAP1, is our experimentally determined parameter. As we show in the Fig. 4c secretion time histograms, the time lag between the predicted

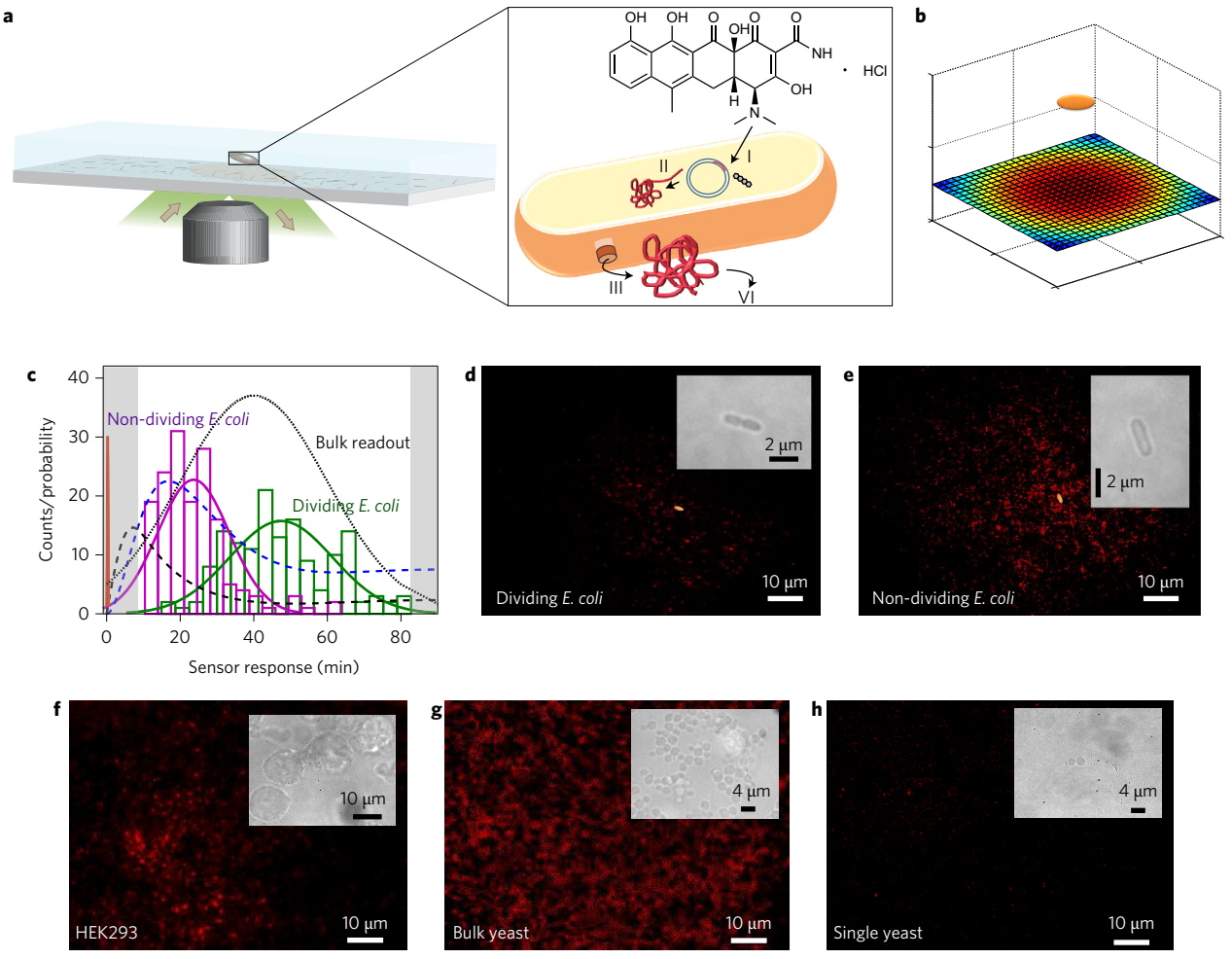

Figure 4 | Imaging the secretion of single proteins from individual microorganisms. a, Schematic of single immobilized *E. coli* above a RAP1-specific nanosensor array surface. The zoom-in of the cell shows four stages of protein production: (I) induction with aTc, (II) transcription and translation, (III) diffusion to the secretion site and secretion, and (IV) diffusion from the secretion site to the nanosensor array. **b**, Model of expected RAP1 protein secretion 'footprint' from an *E. coli* cell above the nanosensor array surface, with a red-blue heat map corresponding to predicted areas of high-low relative protein detection from the *E. coli* source above. **c**, Typical protein footprint 1 h post-induction with aTc of RAP1 secretion for a histogram (counts) of first-response times for each cell for $N = 22$ individual protein secretion events for dividing (green) or non-dividing (magenta) cells, showing quicker first-protein-secretion events for non-dividing cells. Kinetic model for the protein secretion pathway for RAP1 secretion: aTc diffusion to the cell (red spike), protein transcription (mRNA concentration, dashed black) and protein translation (protein concentration, dashed blue). Our assay has the unique capability to discern the kinetic variation. The black dotted line models the expected protein content in the cell supernatant if measured experimentally using an SDS-PAGE gel to monitor for protein band intensity. **d**,**e**, Typical nIR protein footprint 1 h post-induction with aTc of RAP1 secretion for a dividing *E. coli* cell (**d**, bright-field inset) and a non-dividing cell (**e**, bright-field inset). Dividing cells show a noticeably smaller protein secretion footprint than non-dividing cells (154.0 ± 69.2 versus 486.2 ± 113.0 protein-responding sensors, respectively). **f**–**h**, Our device can also be functionalized with sensors that specifically detect HIV-1 integrase proteins. We use a microfluidic device for HIV1 integrase detection to monitor HIV1 integrase protein secreted from HEK cells (**f**), bulk yeast cells (**g**) and a single yeast cell (**h**), with bright-field insets for each. Sensor device can measure protein secretion from a variety of different cell types and measure differences in protein secretion patterns and kinetics.

RAP1 protein synthesis and observed secretion represents the time required for protein secretion from our *E. coli* cell. Finally, step IV represents the diffusion of RAP1 from its secretion point along the cell membrane to the nanosensors array. RAP1 diffusion from point source (the *E. coli* cell) to sensor (the nanosensor array) contributes minimal time to the secretion process (~12 s) and is expected to produce a spatial distribution along the nanosensor array, as modelled by the Brownian diffusion of RAP1 protein from the cell to the surface (Fig. 4b). The kinetics described here and the spatial distribution model are described in Supplementary equations (1) to (5).

Our ability to observe protein secretion from an individual *E. coli* cell enables us to quantify the protein secreted by individual *E. coli* cells by counting the net number of responsive sensors under each cell: the *E. coli* 'protein footprint'. We studied the protein footprint of $N = 22$ cells, where each footprint was formed by the intensity response of each sensor for 1 h from induction with aTc in starved conditions with minimal media. None of the cells studied underwent cellular division, and most did not elongate significantly during the experiment. However, 6 of the 22 cells showed noticeable formation of an invaginated septal wall throughout the course of the experiment (Fig. 4d). Cells showing no signs of cell division were found to have larger protein secretion footprints in the nanosensors array than cells undergoing cell division, as observed by the protein footprint under each cell type (Fig. 4e). Non-dividing cells produced an average of 486.2 ± 113.0 protein-responsive sensors, as compared to the 154.0 ± 69.2 response from sensors that responded underneath dividing cells.

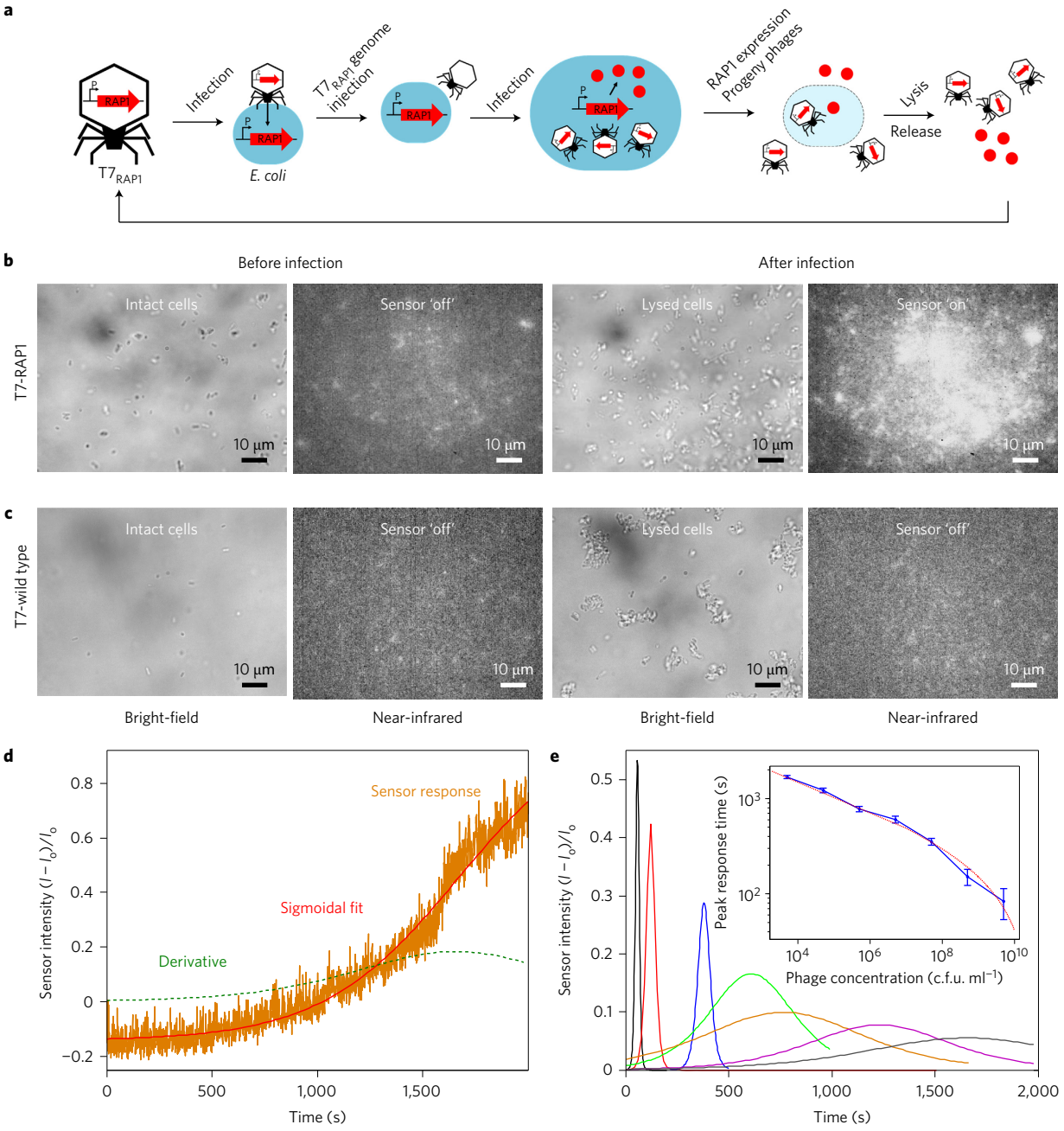

Figure 5 | Real-time monitoring of bacteriophage $T7_{RAP1}$ infection of *E. coli* cells and resulting cell lysis. a, Schematic of $T7_{RAP1}$ infection and lytic cycle of *E. coli*, culminating with cell lysis and release of RAP1 protein. **b**, Bright-field (left) and nIR images (right) of 5×10^{10} c.f.u. ml^{-1} *E. coli* cells prior to ('before infection') and post ('after infection') addition of 5×10^{9} p.f.u. ml^{-1} $T7_{RAP1}$. **c**, Corresponding bright-field and nIR images of 5×10^{10} c.f.u. ml^{-1} *E. coli* cells prior to ('before infection') and post ('after infection') addition of $5 \times e^{9}$ p.f.u. ml^{-1} $T7_{WT}$. Although bright-field can detect lytic infection via *E. coli* lysis, nIR protein sensors detect the RAP1 protein product from phage genome infection. **d**, Concentration–response curve for 5×10^{10} c.f.u. ml^{-1} *E. coli* and 5×10^{6} p.f.u. ml^{-1} $T7_{RAP1}$ (orange), fit to a sigmoid (red), and the corresponding first time-derivative of the sigmoid (green dotted line). **e**, Peak of first-derivatives of 5×10^{10} c.f.u. ml^{-1} *E. coli* and 5×10^{4} (grey), 5×10^{5} (magenta), 5×10^{6} (orange), 5×10^{7} (green), 5×10^{8} (blue) and 5×10^{9} (red) 5×10^{10} (black) p.f.u. ml^{-1} $T7_{RAP1}$. Error bars respresent s.e. Sensors can distinguish between infections that produce target RAP1 proteins and infections that do not.

We next monitored the secretion of a second unlabelled protein product, HIV1 integrase, from both HEK 293 and *P. pastoris* cells. HEK cells were seeded into our microfluidic device in Dulbecco's modified Eagle's medium supplemented with 10% fetal bovine serum and 1% penicillin/streptomycin. HEK cells were monitored for 75 min and the protein footprint underneath a collection of HEK cells was quantified. HEK cells constitutively secreted HIV1 integrase, which we monitored for the duration of the image acquisition. In addition, we monitored HIV1 integrase secretion from *P. pastoris* cells by transferring cells into induction medium BMMY to initiate HIV1 integrase protein production. *P. pastoris* cells were monitored for 75 min both at bulk-cell and single-cell levels, and the secreted HIV1 protein footprint was quantified throughout the course of the image acquisition. For bulk-cell levels (Fig. 4f), HIV1 integrase constitutively secreted from HEK cells 24 h post-trypsinization was monitored. Trypsinized HEK cells were seeded into the device for a duration of 75 min of constitutive secretion. In these trials, HIV1-secreting HEK cells produced

an average intensity turn-on response of 76.0 ± 27% from the HIV1 integrase-specific protein sensor array. Also for bulk-cell levels (Fig. 4g), HIV1 integrase secreted from *P. pastoris* cells was monitored from the time that *P. pastoris* cells were seeded into the device with induction medium BMMY to initiate HIV1 integrase protein production, for a duration of 75 min post-induction. In these trials, HIV1-secreting *P. pastoris* cells produced an average intensity turn-on response of 170.3 ± 32%, from the HIV1 integrase-specific protein sensor array. Single-cell levels of protein secretion were not detected from a single HEK cell seeded into a microfluidic HIV1 integrase sensor device within a 75 min time window. However, single-HIV1 integrase proteins were successfully detected for single *P. pastoris* cells within a 75 min time window (Fig. 4h). Further time-lapse analysis shows that HEK cells showed greatest protein efflux 24 h post-trypsinization, whereas *P. pastoris* cells began to secrete protein on average 30 min post-induction.

Real-time detection of virally induced cell lysis

We engineered a T7 bacteriophage to express RAP1 ($T7_{RAP1}$). Due to the lytic cycle of the T7, we expect a sudden release of RAP1 protein from infected *E. coli* cells undergoing lysis. We used our sensor platform to study the release of RAP1 from the resulting lysis of *E. coli* infected with $T7_{RAP1}$, for varying concentrations of engineered phage. The ratio between the virus particles and bacteria is defined as the MOI, which dictates the infection rate for phage infections:

$$\mathrm{MOI} = \frac{N_{\mathrm{virus}}}{N_{\mathrm{bacteria}}} \tag{1}$$

We can statistically calculate the number of *E. coli* cells that will be infected by a phage for a given MOI with a Poisson distribution[21], where *P(n)* is the probability that a single *E. coli* will be infected by *n* phages for a given MOI, abbreviated *M*:

$$P(n) = \frac{M^n \mathrm{e}^{-M}}{n!} \tag{2}$$

A MOI of 1 defines a closely synchronized infection, and, theoretically, all the host cells are infected at the same time and multiply, where each infection produces about 200 new viruses[22]. Therefore, we chose to perform a series of experiments where the MOI is varied from 10 to 1×10^{-5} and studied the real-time release of RAP1 resulting from *E. coli* lysis.

The fluorescence of surface-immobilized sensors was monitored for up to 1 h, where experiments with lower viral loads showed a longer lysis time. Figure 5a shows a schematic of the T7 bacteriophage infection pathway, culminating with cell lysis and RAP1 release. Figure 5b shows the bright-field images and nIR response of our RAP1 sensors before and after *E. coli* infection by $T7_{RAP1}$. Post-infection, we observe mostly lysed cells and a strong nIR fluorescence increase across the field of view, suggesting RAP1 release. Similarly, Fig. 5c shows the bright-field images and the nIR response of our RAP1 sensors before and after *E. coli* infection by phage lacking the RAP1 gene, $T7_{WT}$. Post-infection, we observe mostly lysed cells in our bright-field channel, but lack a nIR sensor response. These results show the advantage of a protein sensor platform in its ability to detect the specific protein product of a phage infection, instead of only reporting cell lysis.

We performed an analysis of each *E. coli*/$T7_{RAP1}$ ratio and the normalized sensor surface intensity response to each condition as a function of time (Fig. 5d). We notice that the sensor response as a function of post-infection time is sigmoidal, with a clear intensity inflection shortly after addition of $T7_{RAP1}$ for high phage concentrations (5×10^9 p.f.u. ml^{-1}) (p.f.u., plaque-forming units). Similarly, the sensor response is also sigmoidal after the addition of less $T7_{RAP1}$ (5×10^3 p.f.u. ml^{-1}). However, the inflection is slower and therefore less marked at lower phage concentrations. Therefore, to describe both the $T7_{RAP1}$ infection peak and breadth, sensor intensity response curves were analysed by fitting the curve to a sigmoid, where the point of inflection was determined by taking the first time derivative of the sigmoidal fit.

$$\frac{\mathrm{d}I_{\mathrm{norm}}}{\mathrm{d}t} = \left(\frac{1}{1+\mathrm{e}^{-t}}\right)^2 \mathrm{e}^{-t}(-1) = \left(\frac{1}{1+\mathrm{e}^{-t}}\right)\left(\frac{1}{1+\mathrm{e}^{-t}}\right)(-\mathrm{e}^{-t}) = I(t)(1-I(t)) \tag{3}$$

The resulting derivative function can be fit with a Gaussian, where the peak represents the greatest rate of RAP1 protein release from cells lysed due to viral infection. The peak of each Gaussian represents the time point of most *E. coli* lysis and RAP1 release in our microfluidic chamber. A representative response trace with sigmoidal fit and derivative Gaussian is presented in Fig. 5d. As expected, we show that the first derivatives of the sensor intensity response curves are sharply peaked Gaussians at short timescales for our highest bacteriophage dilution, 5×10^9 p.f.u. ml^{-1} (Fig. 5e). As the viral load decreases in order-of-magnitude increments, the first-derivative peaks broaden and peak at longer times, suggesting that the *E. coli* infection process becomes increasingly stochastic and lengthy. We find a primarily linear relationship between peak response time and log-scale phage concentration, suggesting an exponential relationship between viral load and *E. coli* cells for cell lysis.

Conclusions

The design of SWNT-based nanosensors for protein detection from crude and live cell samples requires a robust approach that will produce stable sensors under a variety of conditions optimized for cell viability. To expedite protein detection and push protein detection limits, efforts have turned primarily to electrochemical[23,24], immunosorbent (ELISA)[25], mass spectrometric[26], plasmonic[27–30], fluorescence labelling[7,31] and Raman[32,33] protein and analyte detection techniques. A common limitation faced by these techniques is an inability to simultaneously optimize spatial resolution, temporal resolution or low (single)-protein detection limits, due to non-optical signal transduction. Our results provide an orthogonal approach to discover optical sensors for proteins.

The platform we present here provides label-free protein detection in a wavelength range that enables selective protein recognition in crude samples, from living cells and from bacteriophage-infected cells. Our experimental design accomplishes two key design features for fluorescence-based protein recognition: (1) providing a molecular recognition element for reversible detection of a protein target and (2) maintaining a stable linkage between the SWNT and the molecular recognition element to ensure reproducibility and reversibility of protein detection based on our previous work of polynucleotide corona phase stabilities[34–36]. The selectivity of our protein + aptamer–SWNT screen for RAP1 and HIV1 integrase suggests that, in these two cases, the aptamer serves the purpose of selective protein docking and subsequent perturbation of the SWNT fluorescent corona. We confirm, through the introduction of abasic spacers between the anchor and aptamer sequence, and single-molecule studies, that aptamer denaturation on the SWNT surface is the primary contributor to non-responsive aptamer–SWNT constructs.

We confirm the immediate utility of our platform by addressing the challenge of protein detection from living *E. coli* cells engineered to secrete our target protein. We further extend our platform to detect HIV1 integrase from HEK 293 and *P. pastoris*. *E. coli* is a heavily studied organism for understanding transcription and translation, and for genetic engineering. HEK 293 (human embryonic kidney 293) and *P. pastoris* are widely used eukaryotic protein expression

hosts in both academic laboratories and the pharmaceutical industry. Although intensive efforts have been devoted to improve protein expression through vector design, host cell engineering and upstream process development, there is limited knowledge and experience regarding single-cell analysis of protein secretion. Our approach offers a new way to study eukaryotic protein secretion at the single-cell level and provides insights of protein secretion processes in industrial protein expression systems. Here, we show successful engineering of the RAP1 gene into *E. coli* and the HIV1 integrase gene into HEK 293 and *P. pastoris*. Subsequently, we monitor the productivity of RAP1 and HIV1 integrase protein export by individual engineered *E. coli* and *P. pastoris* cells in real time. For *E. coli,* we show that the process of induction, protein synthesis and protein export is a highly stochastic process yielding variability in protein secretion on a single-cell level, with cells undergoing cell division under starved conditions producing fewer secreted protein products than their non-dividing counterparts. The production of protein products in *E. coli* has been an active area of investigation in recent years, considering both intrinsic and extrinsic sources of protein production fluctuation[37]. Previous studies have indirectly hypothesized that the production of recombinant protein in *E. coli* may be 'diluted' during and immediately following cell division, based on mRNA counts[32]. Others have suggested that cell division could affect transcription rates and gene-regulatory polymerases and ribosomes[38]. Our platform enables direct visualization of net protein production from a single *E. coli* over the course of an hour, confirming both the stochasticity of the process and the effect of cell cycle on the production and export of a recombinant protein product. We further show that our platform can be extended to the detection of protein from *E. coli* infected with T7 bacteriophages carrying the RAP1 gene. Our platform shows the promise of extension for the real-time and single-cell optical detection of a broad range of metabolic products.

Received 20 January 2016; accepted 1 December 2016; published online 23 January 2017

References

1. Keasling, J. D. Synthetic biology and the development of tools for metabolic engineering. *Metab. Eng.* **14,** 189–195 (2012).
2. Kingsmore, S. F. Multiplexed protein measurement: technologies and applications of protein and antibody arrays. *Nat. Rev. Drug Discov.* **5,** 310–320 (2006).
3. Chikkaveeraiah, B. V., Bhirde, A. A., Morgan, N. Y., Eden, H. S. & Chen, X. Electrochemical immunosensors for detection of cancer protein biomarkers. *ACS Nano* **6,** 6546–6561 (2012).
4. Kurita, R., Arai, K., Nakamoto, K., Kato, D. & Niwa, O. Development of electrogenerated chemiluminescence-based enzyme linked immunosorbent assay for sub-pM detection. *Anal. Chem.* **82,** 1692–1697 (2010).
5. Hammock, M. L., Knopfmacher, O., Naab, B. D., Tok, J. B. H. & Bao, Z. A. Investigation of protein detection parameters using nanofunctionalized organic field-effect transistors. *ACS Nano* **7,** 3970–3980 (2013).
6. Jain, A., Liu, R., Xiang, Y. K. & Ha, T. Single-molecule pull-down for studying protein interactions. *Nat. Protoc.* **7,** 445–452 (2012).
7. Jain, A. *et al.* Probing cellular protein complexes using single-molecule pull-down. *Nature* **473,** 484–488 (2011).
8. Mogalisetti, P. & Walt, D. R. Stoichiometry of the α-complementation reaction of *Escherichia coil* β-galactosidase as revealed through single-molecule studies. *Biochemistry* **54,** 1583–1588 (2015).
9. Beyene, A. G., Demirer, G. D. & Landry, M. P. Nanoparticle-templated molecular recognition platforms for detection of biological analytes. *Curr. Protoc. Chem. Biol.* **8,** 197–223 (2016).
10. Salem, D. P. *et al.* Chirality dependent corona phase molecular recognition of DNA-wrapped carbon nanotubes. *Carbon* **97,** 147–153 (2016).
11. Roxbury, D., Mittal, J. & Jagota, A. Molecular-basis of single-walled carbon nanotube recognition by single-stranded DNA. *Nano Lett.* **12,** 1464–1469 (2012).
12. Tu, X. M., Manohar, S., Jagota, A. & Zheng, M. DNA sequence motifs for structure-specific recognition and separation of carbon nanotubes. *Nature* **460,** 250–253 (2009).
13. Bisker, G. *et al.* Protein-targeted corona phase molecular recognition. *Nat. Commun.* **7,** 10241 (2016).
14. Nelson, J. T. *et al.* Mechanism of immobilized protein a binding to immunoglobulin G on nanosensor array surfaces. *Anal. Chem.* **87,** 8186–8193 (2015).
15. Oliveira, S. F. *et al.* Protein functionalized carbon nanomaterials for biomedical applications. *Carbon* **95,** 767–779 (2015).
16. Zhang, J. Q. *et al.* Molecular recognition using corona phase complexes made of synthetic polymers adsorbed on carbon nanotubes. *Nat. Nanotech.* **8,** 959–968 (2013).
17. Yang, R. *et al.* Carbon nanotube-quenched fluorescent oligonucleotides: probes that fluoresce upon hybridization. *J. Am. Chem. Soc.* **130,** 8351–8358 (2008).
18. Kruss, S. *et al.* Neurotransmitter detection using corona phase molecular recognition on fluorescent single-walled carbon nanotube sensors. *J. Am. Chem. Soc.* **136,** 713–724 (2014).
19. Callura, J. M., Cantor, C. R. & Collins, J. J. Genetic switchboard for synthetic biology applications. *Proc. Natl Acad. Sci. USA* **109,** 5850–5855 (2012).
20. Chen, A. Y. *et al.* Synthesis and patterning of tunable multiscale materials with engineered cells. *Nat. Mater.* **13,** 515–523 (2014).
21. Ellis, E. L. & Delbruck, M. The growth of bacteriophage. *J. Gen. Physiol.* **22,** 365–384 (1939).
22. Nguyen, H. M. & Kang, C. Lysis delay and burst shrinkage of coliphage T7 by deletion of terminator Tϕ reversed by deletion of early genes. *J. Virol.* **88,** 2107–2115 (2014).
23. Taleat, Z., Cristea, C., Marrazza, G., Mazloum-Ardakani, M. & Sandulescu, R. Electrochemical immunoassay based on aptamer–protein interaction and functionalized polymer for cancer biomarker detection. *J. Electroanal. Chem.* **717,** 119–124 (2014).
24. Jacobs, C. B., Peairs, M. J. & Venton, B. J. Review: carbon nanotube based electrochemical sensors for biomolecules. *Anal. Chim. Acta* **662,** 105–127 (2010).
25. Rissin, D. M. *et al.* Single-molecule enzyme-linked immunosorbent assay detects serum proteins at subfemtomolar concentrations. *Nat. Biotechnol.* **28,** 595–599 (2010).
26. Shi, T. *et al.* Antibody-free, targeted mass-spectrometric approach for quantification of proteins at low picogram per milliliter levels in human plasma/serum. *Proc. Natl Acad. Sci. USA* **109,** 15395–15400 (2012).
27. Zijlstra, P., Paulo, P. M. R. & Orrit, M. Optical detection of single non-absorbing molecules using the surface plasmon resonance of a gold nanorod. *Nat. Nanotech.* **7,** 379–382 (2012).
28. Anker, J. N. *et al.* Biosensing with plasmonic nanosensors. *Nat. Mater.* **7,** 442–453 (2008).
29. Ament, I., Prasad, J., Henkel, A., Schmachtel, S. & Sonnichsen, C. Single unlabeled protein detection on individual plasmonic nanoparticles. *Nano Lett.* **12,** 1092–1095 (2012).
30. Qian, X. M. *et al. In vivo* tumor targeting and spectroscopic detection with surface-enhanced Raman nanoparticle tags. *Nat. Biotechnol.* **26,** 83–90 (2008).
31. Sakabe, M. *et al.* Rational design of highly sensitive fluorescence probes for protease and glycosidase based on precisely controlled spirocyclization. *J. Am. Chem. Soc.* **135,** 409–414 (2013).
32. Paulus, G. L. C. *et al.* A graphene-based physiometer array for the analysis of single biological cells. *Sci. Rep.* **4,** 6865 (2014).
33. Yang, X., Gu, C., Qian, F., Li, Y. & Zhang, J. Highly sensitive detection of proteins and bacteria in aqueous solution using surface-enhanced raman scattering and optical fibers. *Anal. Chem.* **83,** 5888–5894 (2011).
34. Landry, M. P. *et al.* Comparative dynamics and sequence dependence of DNA and RNA binding to single walled carbon nanotubes. *J. Phys. Chem. C* **119,** 10048–10058 (2015).
35. Giraldo, J. P. *et al.* A ratiometric sensor using single chirality near-infrared fluorescent carbon nanotubes: application to *in vivo* monitoring. *Small* **11,** 3973–3984 (2015).
36. Roxbury, D., Mittal, J. & Jagota, A. Molecular-basis of single-walled carbon nanotube recognition by single-stranded DNA. *Nano Lett.* **12,** 1464–1469 (2012).
37. Elowitz, M. B., Levine, A. J., Siggia, E. D. & Swain, P. S. Stochastic gene expression in a single cell. *Science* **297,** 1183–1186 (2002).
38. Lahav, G. *et al.* Dynamics of the p53-Mdm2 feedback loop in individual cells. *Nat. Genet.* **36,** 147–150 (2004).

Acknowledgements

This work was supported by a Burroughs Wellcome Fund Career Award at the Scientific Interface (CASI), the Simons Foundation, a BBRF young investigator award and a Beckman Foundation Young Investigator Award (to M.P.L.). M.S.S. acknowledges a grant from the National Science Foundation (NSF) to support this work. H.A. is supported by fellowships from the Japan Society for the Promotion of Science and the Naito Foundation. D.Y. acknowledges support from an NSF GRFP fellowship and L.C. acknowledges support from a LAM research fellowship. A.Y.C. acknowledges graduate research support from the Hertz Foundation, the Department of Defense and NIH Medical Scientist Training Program grant T32GM007753. This work was also supported by the National Institutes of Health

(DP2 OD008435 and P50 GM098792), the Office of Naval Research (N00014-13-1-0424) and the NSF (MCB-1350625). The authors thank P. Perez-Pinera (University of Illinois Urbana-Champaign) for providing the parental *Pichia* cells.

Author contributions

M.P.L. and M.S.S. conceived of the aptamer-anchor nanosensor platform and designed experiments. M.P.L. synthesized aptamer–nanotube conjugates, performed protein selectivity screens and carried out *in vitro* and cell-based experiments with J.D. and analysed data. H.A., A.C., J.C. and V.I.K. constructed recombinant *E. coli* strains, H.A. constructed $T7_{RAP1}$ bacteriophage. M.P.L., H.A., A.C., V.I.K., L.C., D.Y., T.K.L. and M.S.S. discussed the experimental results and wrote the manuscript. All authors discussed the results and commented on the manuscript.

Additional information

Supplementary information is available in the online version of the paper. Reprints and permissions information is available online at www.nature.com/reprints. Correspondence and requests for materials should be addressed to M.S.S.

Competing financial interests

The authors declare no competing financial interests.